ACSNANO

www.acsnano.org

ARTICLE

Podosome Force Generation Machinery: A Local Balance between Protrusion at the Core and Traction at the Ring

Anaïs Bouissou,[†,△] Amsha Proag,[†,△] Nicolas Bourg,[‡,§] Karine Pingris,[†] Clément Cabriel,[‡,§] Stéphanie Balor,[∥] Thomas Mangeat,[⊥] Christophe Thibault,[#,□] Christophe Vieu,[#,□] Guillaume Dupuis,[§] Emmanuel Fort,[○] Sandrine Lévêque-Fort,[‡,§] Isabelle Maridonneau-Parini,*[,†,¶] and Renaud Poincloux*[,†,¶]

[†]Institut de Pharmacologie et de Biologie Structurale, Université de Toulouse, CNRS, UPS, Toulouse 31400, France

[‡]Institut des Sciences Moléculaires d'Orsay, Université Paris-Sud, CNRS UMR8214, Orsay 91405, France

[§]Université Paris-Sud, Centre de Photonique BioMédicale, Fédération LUMAT, CNRS, FR 2764, Orsay 91405, France

[∥]METi, Toulouse 31062, France

[⊥]LBCMCP, Centre de Biologie Intégrative, Université de Toulouse, CNRS, UPS, Toulouse 31062, France

[#]CNRS, LAAS, Toulouse 31031, France

[□]Université de Toulouse, INSA, Toulouse 31077, France

[○]Institut Langevin, ESPCI, CNRS, PSL Research University, Paris 75005, France

Supporting Information

ABSTRACT: **Determining how cells generate and transduce mechanical forces at the nanoscale is a major technical challenge for the understanding of numerous physiological and pathological processes. Podosomes are submicrometer cell structures with a columnar F-actin core surrounded by a ring of adhesion proteins, which possess the singular ability to protrude into and probe the extracellular matrix. Using protrusion force microscopy, we have previously shown that single podosomes produce local nanoscale protrusions on the extracellular environment. However, how cellular forces are distributed to allow this protruding mechanism is still unknown. To investigate the molecular machinery of protrusion force generation, we performed mechanical simulations and developed quantitative image analyses of nanoscale architectural and mechanical measurements. First, *in silico* modeling showed that the deformations of the substrate made by podosomes require protrusion forces to be balanced by local traction forces at the immediate core periphery where the adhesion ring is located. Second, we showed that three-ring proteins are required for actin polymerization and protrusion force generation. Third, using DONALD, a 3D nanoscopy technique that provides 20 nm isotropic localization precision, we related force generation to the molecular extension of talin within the podosome ring, which requires vinculin and paxillin, indicating that the ring sustains mechanical tension. Our work demonstrates that the ring is a site of tension, balancing protrusion at the core. This local coupling of opposing forces forms the basis of protrusion and reveals the podosome as a nanoscale autonomous force generator.**

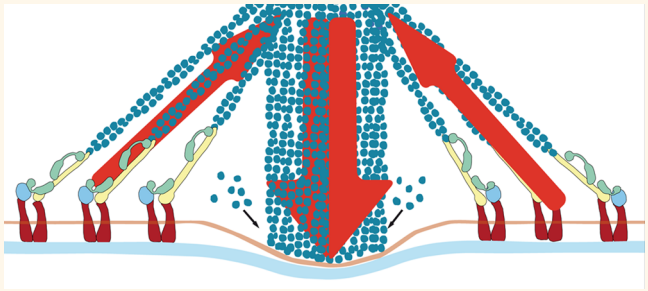

KEYWORDS: *atomic force microscopy, 3D nanoscopy, cell mechanics, protrusion force, podosomes*

Podosomes are submicrometer adhesion cell structures formed at the plasma membrane that protrude into, probe, and remodel the extracellular environment by releasing proteases. Podosomes are formed by macrophages, immature dendritic cells, and osteoclasts, and they also relate to the protrusive structures found in lymphocytes, endothelial cells, invasive tumor cells, and neurons.[1−5] To evaluate the protrusion forces exerted by podosomes, we have developed an atomic force microscopy (AFM)-based method called protrusion force microscopy (PFM) and evidenced that single podosomes are able to deform a thin elastic substrate, producing nanoscale bulges. The forces responsible for these

Received: January 27, 2017
Accepted: March 29, 2017
Published: March 29, 2017

DOI: 10.1021/acsnano.7b00622
ACS Nano 2017, 11, 4028−4040

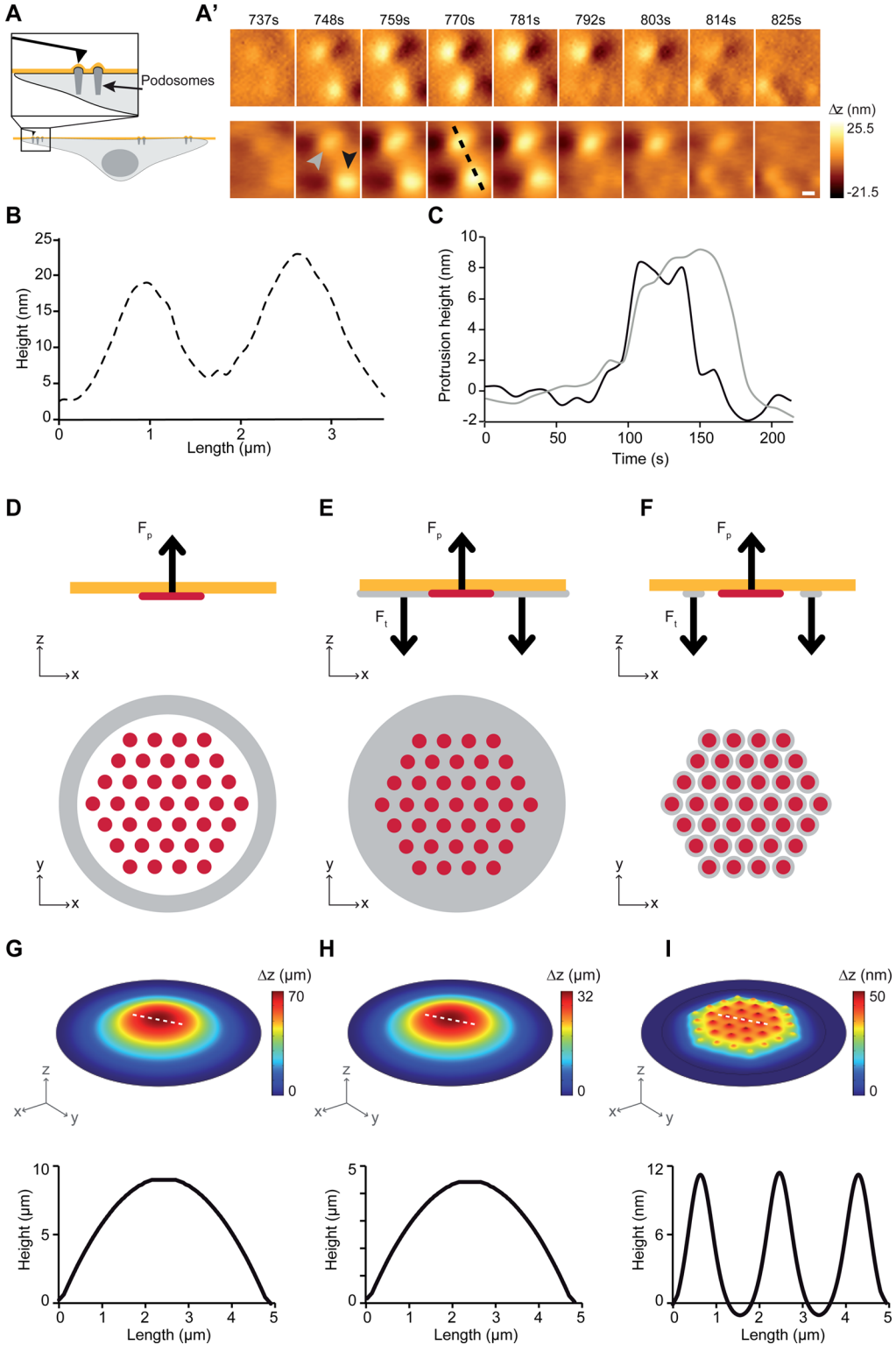

Figure 1. Substrate deformation by single podosomes results from local traction and protrusion. (A) Podosome-induced deformations onto a thin Formvar membrane (yellow). As shown in the scheme, the topography of the membrane is imaged over time by atomic force microscopy (AFM) in contact mode, on the side of the Formvar membrane not in contact with the macrophages. (A′) Two podosome-induced protrusions are shown in the movie stills (upper panel: vertical deflection; lower panel: height; see Movie 1 for the entire sequence and a larger field). Bar: 500 nm. (B) Height profile of the dotted line in (A′). (C) Protrusion height over time of the two protrusions shown in (A) (arrowheads). (D−F) Protrusion−traction model used for the numerical simulation of substrate deformation by podosomes. A circular 16-μm-wide, 30-nm-thick Formvar plate, clamped at its borders, is subjected to local protrusion force, directed against the substrate, and global (D, E) or local (F) traction forces, oriented away from it. Protrusion at each podosome core was modeled as an upward force of 10 nN on the 280-nm-wide red disc. Global traction was modeled as a downward force equal to the opposite total pushing force (370 nN) and applied to the gray area: an annular domain at the periphery of the podosome array (D), or the entire podosome area (E). In contrast, local traction consisted in a 10 nN downward force applied at each ring domain (F). The parameters used for these simulations correspond to typical

DOI: 10.1021/acsnano.7b00622
ACS Nano 2017, 11, 4028−4040

Figure 1. continued

experimental conditions (see Methods). (G–I) Simulation results of the deformation of a Formvar plate by a hexagonal lattice of 37 protrusion–traction modules. Upper panels: deformation map: lower panels: profiles along the dotted lines on the upper panels. Only the local traction configuration produces a deformation profile consistent with experimental measurements.

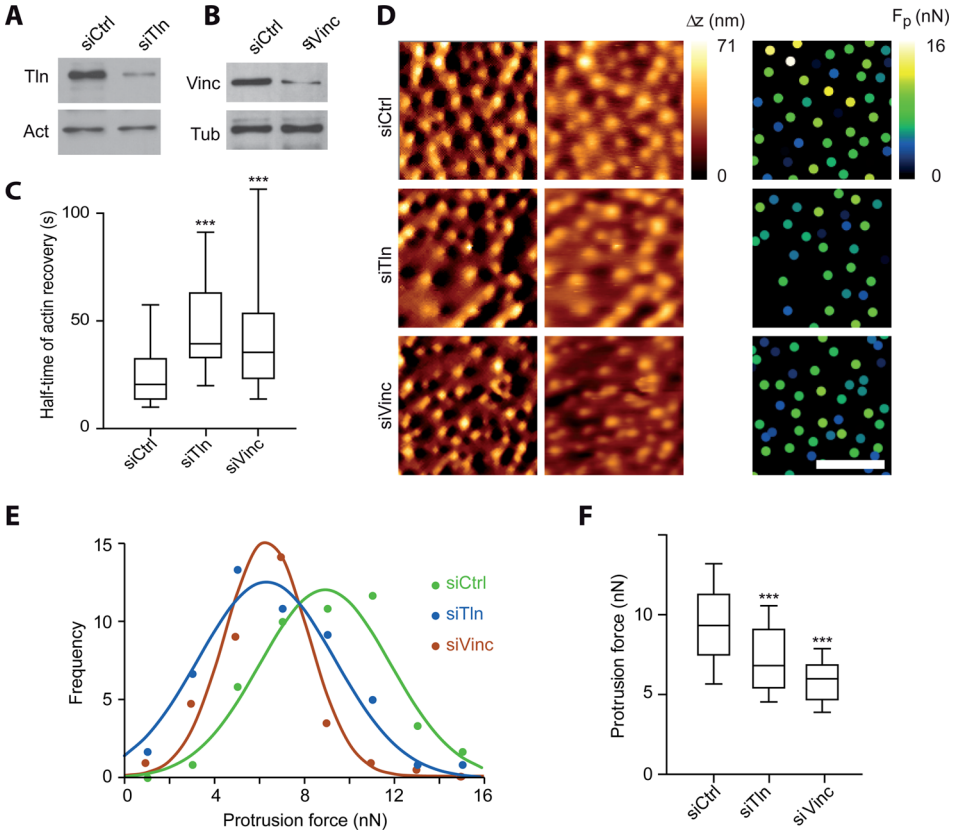

Figure 2. Talin or vinculin knockdown decreases protrusion force and core actin polymerization. (A) Representative Western blot of talin siRNA-mediated depletion out of 5 experiments. (B) Representative Western blot of vinculin siRNA-mediated depletion out of 5 experiments. (C) Actin polymerization rate in the podosome core measured by fluorescence recovery after photobleaching (FRAP) experiments for the different conditions (*n* donors > 3 and *n* podosomes > 29). (D) Left and middle panels: Representative images of the topography of the substrate deformed by podosomes and measured by PFM, showing the vertical deflection (left) and height (middle) for the different conditions. Right panels: Corresponding force maps. Bar: 5 μm. (E) Force distribution of the protrusions shown in (D), fitted by a normal curve. (F) Podosome protrusion force under the different depletion conditions (3 donors, *n* cells > 40, *n* podosomes > 1800). For all graphs, asterisks indicate statistically significant differences compared with control cell populations (see Tables S2 and S3).

deformations increase in response to higher substrate stiffness[6] and require actin polymerization and myosin II activity. How cellular forces are distributed to allow this protruding mechanism at the scale of a podosome is still unknown. We hypothesize that the podosome machinery relies on a local balance of a central protrusion force with a peripheral traction force. Podosomes exhibit a characteristic bipartite architecture with radial symmetry: a core of F-actin and a surrounding adhesion ring composed of integrins and adaptor proteins.[7] This organization suggests that an actin polymerization-driven pushing force would take place beneath the podosome core, while the adhesion ring could bear a counterbalancing pulling force. Supporting this model, several proteins that belong to the ring, such as talin, vinculin, and paxillin, are implicated in traction force transmission in focal adhesions.[8,9]

To provide sound foundations to this model and ascertain that the podosome ring actually transmits cellular traction forces to the substrate, we established a comprehensive link between the nanoscale spatial organization of single podosomes and the mechanical efficiency of this mesoscale structure. We combined state-of-the-art techniques, namely, nanonewton force microscopy and 3D super-resolution optical imaging, and develop a quantitative workflow to investigate molecular architecture and force generation within single podosomes. First, finite-element simulations show that podosomes are sites of local balance between protrusion and traction forces. Then, using PFM we show that three proteins of the podosome ring, talin, vinculin, and paxillin, are needed for the podosome to protrude against the substrate. Finally, using 3D nanoscopy we observed vertical extension of talin, indicating that the ring sustains mechanical tension. These results define the podosome as an autonomous nanoscale protrusion force generator in which adhesion proteins sustain tension and feedback on actin-driven protrusion.

RESULTS

Substrate Deformation by *in Silico* Podosomes Requires Local Traction in Addition to Protrusion. To

DOI: 10.1021/acsnano.7b00622
ACS Nano 2017, 11, 4028–4040

characterize the deformation of the substrate produced by podosomes, we used PFM, which consists in plating human primary monocyte-derived macrophages on a nanometer-thick Formvar elastic membrane and measuring by AFM the nanometer-scale deformations of the substrate (Figure 1A and Movie S1).[6] As a podosome protrudes, the substrate exhibits a 20-nm-high, 2-μm-wide bulge with radial symmetry that oscillates during a few minutes before relaxing back to a flat state (Figure 1B,C). Thus, single podosomes create transient strains in the substrate at the scale of their own size. How cellular forces can generate this deformation profile is not known.

Considering that the podosome is at equilibrium, protrusion forces need to be balanced within the cell to allow the deformation of the substrate: forces directed toward the substrate (pushing forces) should be equilibrated by forces oriented toward the cell (pulling forces). To determine the spatial distribution of these forces, we simulated a hexagonal array of simplified podosome modules acting on a Formvar sheet. The sheet was defined as a 30-nm-thick disc made of a purely elastic material of Young's modulus 2.1 GPa and Poisson ratio 0.3.[6] Each module comprised a 280-nm-wide disc subjected to an upward compression force of 10 nN, an estimation of the pushing forces exerted by a podosome core.[10] Pulling forces were defined according to three different configurations: they were either (i) applied on an annular area at the periphery of the podosome array (Figure 1D), (ii) spread out on the entire podosome area (Figure 1E), or (iii) exerted locally on a circular area around each disc, representing the podosome ring (Figure 1F). Force values were chosen so as to balance total pulling forces with pushing forces. The deformation of the sheet resulting from either of these three load configurations was obtained by solving the linear elasticity equations, where zero displacement was imposed on the circular boundary of the sheet. Only in the case of hypothesis (iii), *i.e.*, local traction, does the resulting deformation display bulges (Figure 1G–I), which are of the same scale as the experimental topography measurements (Figure 1B). This result argues in favor of local traction forces surrounding pushing forces within individual podosomes.

Podosome Ring Integrity Is Required for Protrusive Force Generation. If local traction forces are required for protrusion force generation, we reasoned that specifically disrupting ring integrity should reduce the protrusive capacity of podosomes. We therefore experimentally targeted talin, vinculin, and paxillin, three podosome ring proteins reported in the context of focal adhesions as important to sustain and transmit cellular traction forces,[8,9,11] but whose roles in podosome mechanics have never been investigated. Talin and vinculin are proposed to physically link transmembrane integrins to the actin cytoskeleton. Under tension, talin assumes an unfolded conformation and can recruit, bind, and be stabilized by vinculin.[12−17] Paxillin, although not considered to be a direct adhesion−cytoskeleton link, coordinates cell adhesion dynamics through its interaction with numerous regulatory and structural proteins including integrins and vinculin.[18−20] We knocked down the expression of each of these three proteins in macrophages using a dedicated small-interfering-RNA (siRNA)-based protocol.[21] To estimate the depletion of the protein of interest in macrophages treated with siRNAs, we performed Western blot experiments. siRNA treatments resulted in a 62 ± 6% talin depletion (mean ± SEM), a 75 ± 6% vinculin depletion, and an 88 ± 6% paxillin depletion (Figure 2A,B). We then verified the localization of the proteins remaining after siRNA-mediated depletion. The talin-, vinculin-, and paxillin-depleted macrophages (called siTln, siVinc, and siPax, respectively) still formed podosomes, albeit with less talin, vinculin, or paxillin staining at the ring than control cells (called siCtrl) (Figure S2). Of note, cell spreading area and podosome density and stability were affected in siTln and in siPax but not in siVinc macrophages (Figure S3, S4A,B, and Movie S2).

We evaluated the protrusion forces generated by macrophage podosomes by two approaches. First, we measured the rate of actin polymerization at the core, which is known to power protrusion in podosomes.[6] For this purpose, we quantified fluorescence recovery (FRAP) after photobleaching single podosomes in macrophages expressing actin-RFP. The depletion of each of the three proteins increased the recovery half-time, indicating slower actin polymerization (Figures 2C and S1B). Second, we used PFM to evaluate the forces exerted on the substrate by podosomes (Figure 1A).[6,10] Deformation profiles obtained from AFM topography measurements (Figures 2D and S1C, left and middle panels) are converted into force values based on the model of the protrusion−traction module (Figure 1F), taking into account podosome size and Formvar film thickness to supply the required geometrical parameters (Figures 2D (right panels), 2E, S1C,D).[10] To obtain the parameters corresponding to the depleted conditions, we measured podosome geometry from deconvolved fluorescence images of immunostained unroofed macrophages. Podosomes were indeed respectively 35% and 11% larger in siTln and siVinc cells compared to siCtrl, whereas they were 11% smaller in siPax cells (Figure S3C). Next, PFM measurements were performed on three separate donors on about 2000 podosomes per condition. They showed lower forces exerted on the substrate in cells depleted of ring proteins, compared to siCtrl cells (Figure 2F and Figure S1E). Thus, these ring proteins are important for actin polymerization-driven force generation and for force transmission to the substrate.

As the vinculin−paxillin interaction requires paxillin phosphorylation on residues Y31 and Y118 by FAK in response to myosin contractility,[20] we tested whether paxillin activity was involved in protrusion force activity. For this, we subjected cells to PF-562,271, a drug that specifically inhibits the phosphorylation of the focal adhesion kinase FAK and the related kinase PYK2 and subsequently inhibits paxillin phosphorylation.[22] Treating cells with PF-562,271 inhibited paxillin phosphorylation in macrophages (Figure S5A) and decreased protrusion forces similarly to paxillin depletion (compare Figure S5B−D with Figure S1C−E). Hence, protrusion force generation requires the signaling activity of paxillin.

Overall, the three tension-sensitive ring proteins talin, vinculin, and paxillin are required for core actin polymerization and protrusive force generation. This demonstrates the importance of ring integrity for the podosome to protrude and also suggests that tension may be exerted at the ring.

3D Nanoscopy Reveals Talin Vertical Extension in the Podosome Ring. Tension in the adhesion ring should translate into a molecular deformation of the podosome organization. Indeed, tension has been correlated with talin vertical extension in focal adhesions.[23−25] Since our experiments show talin to be involved in the force machinery of the podosome, we hypothesized that it could be vertically extended

DOI: 10.1021/acsnano.7b00622
ACS Nano 2017, 11, 4028−4040

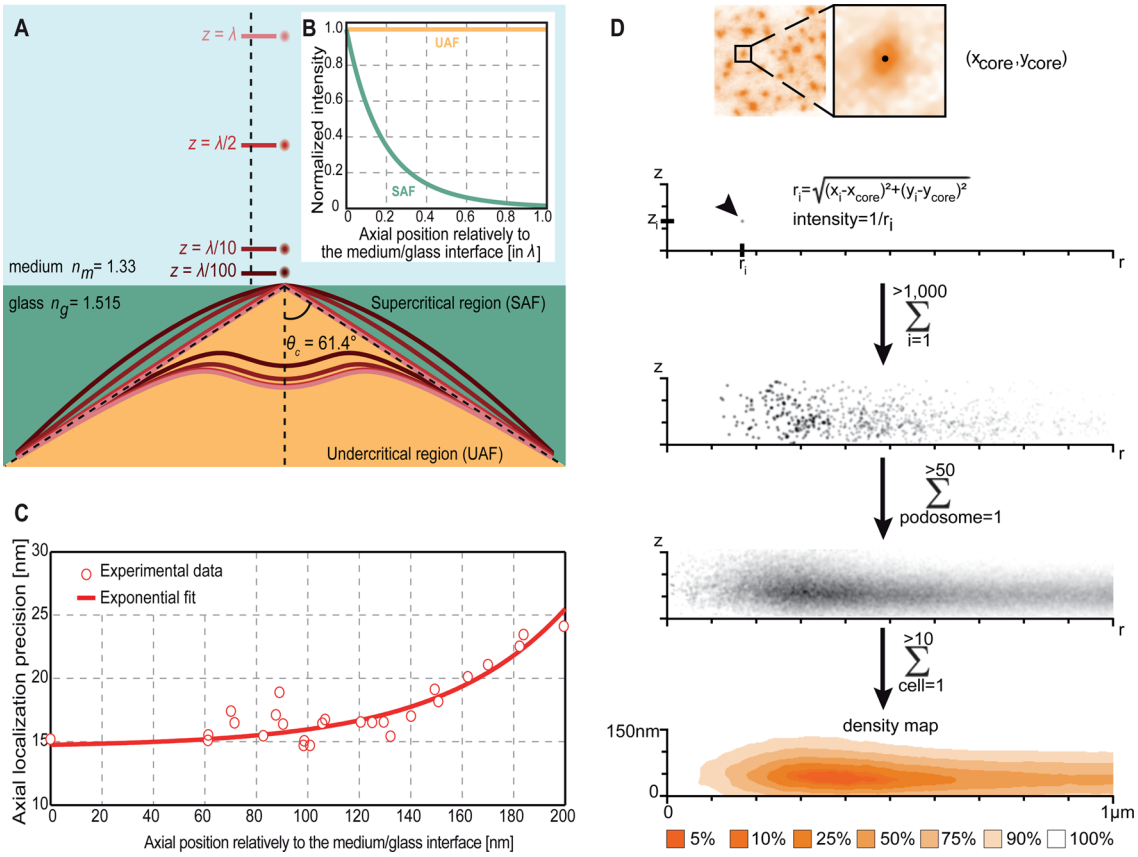

Figure 3. Quantitative 3D nanoscale localization of podosome ring components by DONALD imaging. (A) The fluorescence of a molecule located in the near-field region (z = 0 to λ_{em}) collected by a high numerical aperture objective (NA = 1.49) has two components: the far- and the near-field components. The far-field emission component, also called undercritical angle fluorescence (UAF), has an angular distribution determined by the law of refraction and limited by the critical angle θ_c. This angular distribution of light can be retrieved in the back focal plane (BFP) within a disk of diameter Φ_c, which is related to θ_c. A portion of the near-field emission component that is initially evanescent becomes propagative beyond the critical angle θ_c inside the glass. This part of the fluorescence light, which is also called supercritical angle fluorescence (SAF), can be retrieved in the BFP within a ring shape surrounding the UAF disk (angular distribution of the emission based on ref 40). (B) Whereas the number of UAF photons N^{UAF} remains nearly constant as a function of the interface−fluorophore distance z, the number of SAF photons N^{SAF} decreases approximately exponentially.[40] Hence, the simultaneous measurement of N^{SAF} and N^{UAF} and computation of the fluorophore SAF ratio $\rho^{SAF} = N^{SAF}/N^{UAF}$ for each detected fluorophore can be used to determine the absolute axial position z of the fluorophore. (C) The axial localization precision was measured on 20 nm red beads randomly embedded in 3% agarose gel (n_m = 1.33). Several beads of various depths from several fields of view were sequentially imaged in an emission regime similar to Alexa Fluor 647 in terms of signal-to-noise ratio and axially superlocalized thanks to the DONALD technique. For a given bead, the experimental axial localization precision (red circled dots) is the standard deviation of the series of axial superlocalization measurements given by the DONALD technique. At this level of signal-to-noise ratio, the axial localization precision deteriorates slowly with depth (from 15 nm for $z \approx 0$ to 25 nm for $z \approx 200$ nm). (D) To build the radial height probability density $f(r, z)$ for a single podosome, each protein molecule of coordinates (x_i, y_i, z_i) detected around a given podosome core (x_{core},y_{core}) was plotted on an r−z map at coordinates (r_i, z_i) with an intensity of $1/r_i$. The superposition of all such points yielded $f(r, z)$ after normalization. Radial height probability density maps were then averaged over more than 50 podosomes per cell, then over all cells, and finally over all donors. In the final representation, each region was determined as the region of smallest area that encloses the indicated proportion of the proteins: the smallest regions are thus the most concentrated.

in the podosome ring and sought to measure its structural deformation.

For this purpose, we used a powerful super-resolution technique called direct optical nanoscopy with axially localized detection (DONALD) that combines direct stochastic optical reconstruction microscopy (dSTORM) with supercritical angle fluorescence (SAF).[26,27] This enables the detection of single fluorophores with a lateral localization precision of typically 5 to 10 nm and an absolute vertical position with a precision of 15 nm (Figure 3A−C). We developed a systematic workflow to obtain a quantitative map of the spatial organization of the podosome components localized by DONALD. It consists in calculating the probability density function $f(r, z)$ of the height and radius of each protein detected, with respect to the actin core stained on the same cells. Each protein molecule of coordinates (x_i, y_i, z_i) detected around a given podosome core (x_{core}, y_{core}) was plotted on an r−z map at coordinates (r_i, z_i) with an intensity of $1/r_i$. The superposition of all such points yielded $f(r, z)$ after normalization (Figure 3D). Single-podosome density maps were then averaged over thousands of podosomes, ultimately yielding an average podosome characterized by the probability density of the radial and vertical position of each component analyzed.

We performed DONALD imaging of human macrophages to obtain the distance of talin molecules to the substrate (*i.e.*, the height) (Figure 4A). Paxillin and actin were also localized as reference markers for the core and the ring. To evaluate talin vertical extension, we adapted the approach of Kanchanawong

DOI: 10.1021/acsnano.7b00622
ACS Nano 2017, 11, 4028−4040

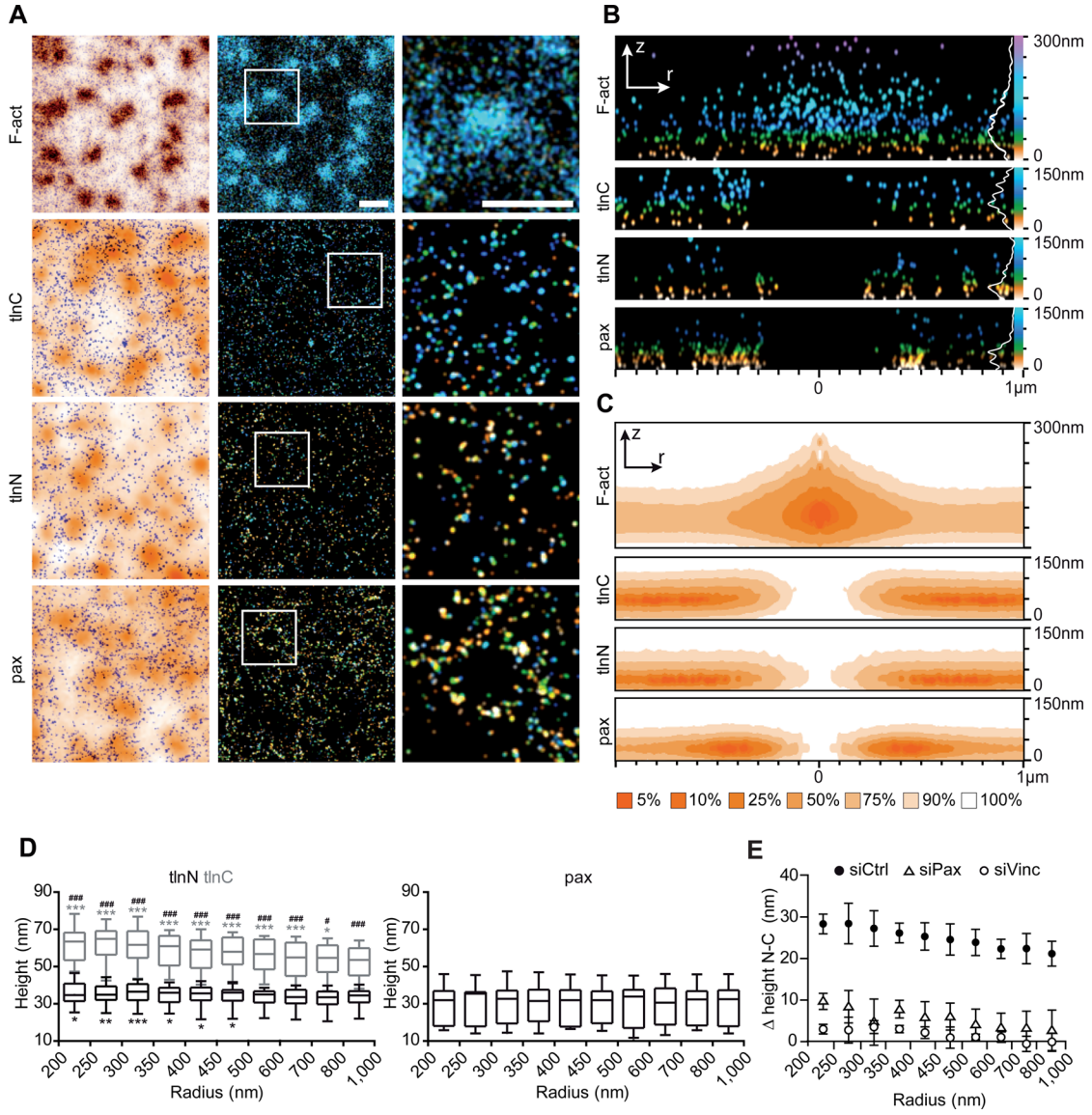

Figure 4. Talin is vertically extended in the podosome ring. (A) Left panels: Representative dSTORM images of, from top to bottom, F-actin (F-act), talin-C (tln *C*), talin-N (tln *N*), and paxillin (pax) (purple) merged with the corresponding epifluorescence images of the F-actin core (ochre). Middle panels: Corresponding DONALD images where the height is represented in false color (scale shown in (B)). Right panels: Enlargement of the framed podosomes. Bar: 1 μm. (B) Localization of F-actin, talin-C, talin-N, and paxillin within single podosomes. For each protein, the orthogonal sections of the podosomes enlarged in (A) are shown with the height distribution (white curve on the right side). In these radial height profiles, color corresponds to the height *z* and intensity denotes the density of detected protein in the *r*−*z* space. (C) Probability density maps of the radial and vertical position of the detected proteins. Each region has been determined as the region of smallest area that encloses the indicated proportion of protein: the smallest region is thus the most concentrated (*n* donors > 3, *n* cells > 11, *n* podosomes > 1200). (D) Height profiles of the ring proteins with respect to the distance to the center of the actin core. Black/gray asterisks indicate when a distance class is significantly different from the [800; 1000] nm class. Hash signs indicate statistically significant differences between the height of talin-N and talin-C within each distance class (see Table S4). (E) Height difference between talin-C and talin-N for each distance class in siCtrl cells (filled circles, mean ± SD), siVinc cells (open circles), and siPax cells (open triangles) (*n* donors > 3, *n* cells >19, *n* podosomes > 1500).

and co-workers[23] and imaged it twice using antibodies directed toward residues 434−1076 in its N-terminal region (hereafter called talin-N) and residues 2522−2541 at its C-terminal extremity (talin-C). Radial height profiles and density maps show that paxillin and talin-N localized in a narrow layer close to the substrate (31 ± 3 and 35 ± 1 nm, respectively), which corresponds to the expected vertical position of the integrin intracellular domains.[23,28] Talin-C, however, displayed a higher and broader vertical distribution centered around 61 ± 2 nm, *i.e.*, 26 nm higher than talin-N (Figure 4B−D). This value compares well with the distance previously observed in focal adhesions that has been correlated to an extended conformation.[16,23,29] Talin-C also showed an increasing height profile toward the core, and the height difference between talin-N and talin-C was correspondingly greater in the ring (Figure 4D). This suggests that talin might display different conformations in podosomes: a folded conformation far from the actin cores and a stretched conformation close to the cores. Actually, it is likely that talin displays not only two conformations but rather a continuum of stretched conforma-

DOI: 10.1021/acsnano.7b00622
ACS Nano 2017, 11, 4028−4040

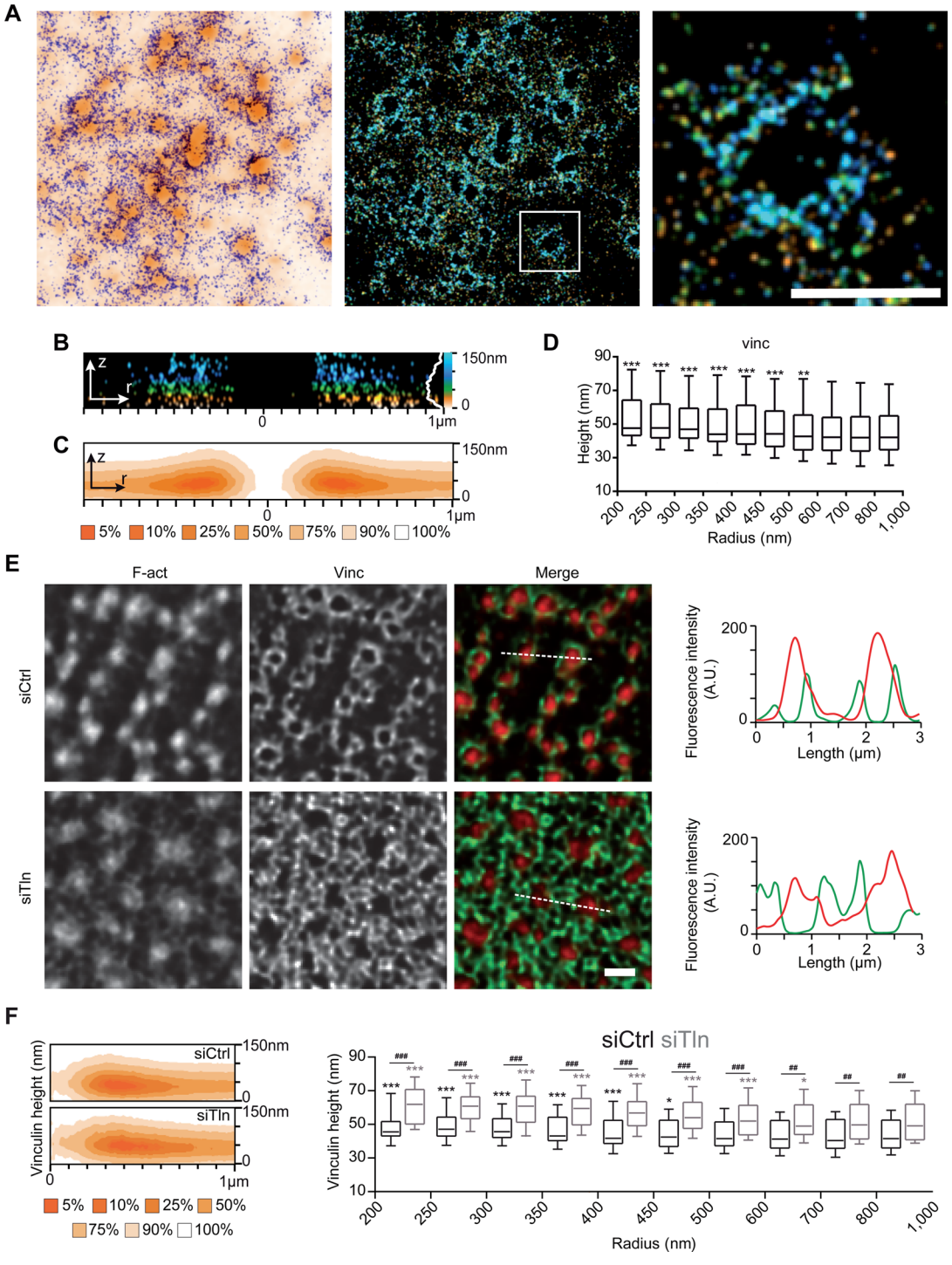

Figure 5. Vinculin localization is associated with talin extension at the ring. (A) Left: Representative dSTORM images of vinculin (purple) in podosomes merged with the corresponding epifluorescence images of the F-actin core (ochre). Middle: Corresponding DONALD image where the height is represented in false color (scale shown in (B)). Right: Enlargement of the framed podosome. Bar: 1 μm. (B) Localization of vinculin within single podosomes. The orthogonal section of the podosome enlarged in (A) is shown with the height distribution (white curve). Color corresponds to the height z. (C) Probability density maps of the radial and vertical position of vinculin. Each region has been determined as the region of smallest area that encloses the indicated proportion of protein: the smallest region is thus the most concentrated (7 donors, 41 cells, n podosomes > 4000). (D) Vinculin height profile with respect to the distance to the center of the actin core. Asterisks indicate statistically significant differences between each distance class and the [800; 1000] nm class. (E) Left: Representative immunofluorescence images of podosomes of siCtrl and siTln macrophages co-immunostained for F-actin (red) and vinculin (green). Right: Intensity profiles along the dotted lines. Bar: 1 μm. (F) Left: Radial probability density maps showing the volume distribution of vinculin in the $r-z$ space in siCtrl and siTln cells. Right: Height profiles of vinculin with respect to the distance to the center of the actin core in siCtrl cells *versus* siTln cells. Black/gray asterisks indicate when a distance class is significantly different from the [800; 1000] nm class, whereas hash signs denote the difference between vinculin height in siCtrl cells *versus* siTln cells (see Table S4) (n donors > 4, n cells > 31, n podosomes > 2300).

DOI: 10.1021/acsnano.7b00622
ACS Nano 2017, 11, 4028−4040

tions depending on the traction intensity, as suggested by *in vitro* experiments.[14,30] Overall, talin is vertically oriented and extends on average over 26 nm, which suggests that talin is under tension.

Vinculin and Paxillin Stabilize Talin Extension. We then wanted to confirm that the observed talin orientation resulted from tension applied in the adhesion ring. Having shown that ring integrity is required for protrusion force, we examined the effect of vinculin and paxillin depletion on talin extension. The average difference between the *z*-positions of talin-C and talin-N was reduced from 26 nm in siCtrl cells to less than 4 nm in siVinc cells and to 6 nm on average in siPax cells (Figure 4E). Hence, vinculin and paxillin are required for talin extension in podosomes, which further supports the existence of tension in the podosome ring.

Since vinculin and paxillin depletion reduce both force generation and talin vertical extension, the deformation we reveal here within the adhesion ring probably results from a traction force that pulls on the substrate at the contact area and counterbalances the protrusion force developed at the core against the substrate.

Vinculin Localization Is Associated with Talin Extension at the Ring. Finally, to further support a traction force at the adhesion ring as indicated by talin extension, we determined nanoscale vinculin localization. Indeed, it has been proposed that, when subjected to tension, talin exposes sites where vinculin can bind, thus stabilizing the mechanical linkage between integrins and the actin cytoskeleton.[12,14,31] Hence, talin extension in podosomes should correlate with vinculin recruitment at the ring. We therefore assessed the nanoscale localization of vinculin using DONALD imaging (Figure 5A). Radial height profiles and density maps yield a broad height distribution with an average localization at 52 ± 3 nm above the substrate, remaining between the height values of talin-N (35 nm) and talin-C (61 nm). This wide vertical distribution of vinculin within single podosomes may indicate the presence of several populations of vinculin molecules that bind either directly to different sites on the talin molecules or to other partners such as integrins, paxillin, or actin. Strikingly, vinculin height varied with respect to the distance to the core, correlating with the observed talin extension: it increased gradually from 46 ± 3 nm to over 54 ± 3 nm when close to the core (Figure 5B–D). To assess whether vinculin localization at the ring actually depends on talin, we imaged vinculin in talin-depleted macrophages. In this condition, vinculin did not present the typical ring morphology, but instead was displaced farther from the podosome core into the space between podosomes (Figure 5E,F). Furthermore, vinculin vertical localization in siTln cells was higher compared to siCtrl cells (Figure 5F), suggesting that, in the absence of talin, vinculin may bind to other partners, such as actin. Hence, talin controls vinculin nanoscale localization at the ring.

In summary, the podosome ring proteins, talin, vinculin, and paxillin, are important for protrusion force generation, and talin presents a vinculin- and paxillin-dependent extension that correlates with vinculin recruitment at the ring. These results support the notion that traction at the ring and protrusion at the core sustain each other, resulting in local substrate deformation by the podosome (Figure 6).

DISCUSSION

Combining finite element simulations, force measurements by PFM, and the nanoscale 3D organization data obtained with DONALD, we provide evidence that the generation of protrusions by podosomes requires both protrusive force at the core and traction force at the adhesion ring. Thus, this work brings forward highly significant and original data for podosome mechanics. Indeed, it demonstrates that podosomes are autonomous force generators where adhesion ring proteins regulate the protrusion generator at the core and sustain the resulting mechanical tension so that force is transmitted to the substrate (Figure 6). This supports a mechanical coupling between core and ring and provides a mechanism for local mechanotransduction, in the sense that tension-based rigidity sensing could feedback on protrusion dynamics. Such a coupling could also explain why the levels of core actin and ring components are correlated.[32,33]

We provide a 3D portrait of the podosome, which calls for a deeper inquiry into the underlying molecular actors that couple the core to the ring. The radial profiles we observed for talin vertical extension and for vinculin height provide a hint toward the scaffold underlying this coupling. Indeed, both profiles increase similarly by 10 nm near the core, while the talin-N position remains uniform. This may result from two nonexclusive causes. On one hand, talin could be more stretched near the core and vinculin would then have access to the binding sites closer to the C extremity of the talin molecule.[14,31] On the other hand, traction force could also steepen talin orientation close to the core, while vinculin would remain bound at a fixed position on talin. Both phenomena require a force with a vertical component to be exerted on talin molecules. Since the C extremity of talin is able to bind actin, the linkage could be embodied by lateral actin filaments (Figure 6).[34]

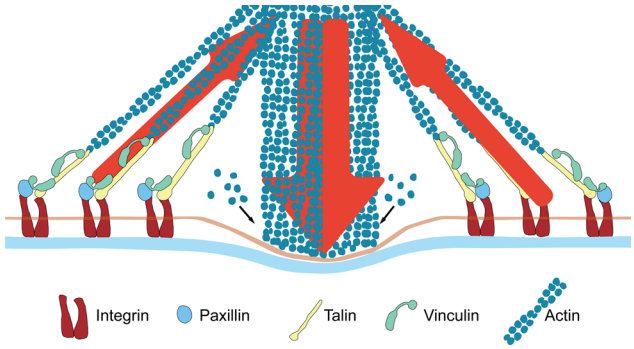

Figure 6. Model of ring protein organization and podosome force generation. Based on the current knowledge and our results on podosomes, we propose the following model. At the core of the podosome, F-actin polymerizes against the substrate; it is surrounded by a spatially structured ring-shaped integrin-based adhesion complex. Paxillin and talin, known to bind to the intracellular domains of integrins, were found about 30 nm above the substrate. Talin assumes an open conformation under traction probably mediated by lateral actin filaments, all the more stretched as it nears the core. This tension-dependent stretching has been shown to uncover multiple vinculin-binding sites on the talin molecule and thus enables, in podosomes, the binding of vinculin, which in turn stabilizes talin extension. Hence protrusion at the core, driven by actin polymerization (central arrow), is balanced by traction at the ring (lateral arrows), sustained and transmitted to the substrate by talin, which is required for protrusive deformation of the substrate. Talin, vinculin, and paxillin act together, at a specific place in the ring, to respond to tension by enabling efficient force generation on the environment.

DOI: 10.1021/acsnano.7b00622
ACS Nano 2017, 11, 4028–4040

Interestingly, this hypothesis would make a similarity between podosomes and focal adhesions, despite their different organization and mechanics. Focal adhesions are elongated adhesive plaques where acto-myosin-dependent traction forces are applied tangentially to the substrate and counterbalanced at the scale of the whole cell, whereas podosomes are circular bipartite structures capable of protruding into the substrate through local force generation. However, our nanoscopy data show that podosomes possess similar molecular architecture to focal adhesions.[23] This makes it reasonable to think of lateral actin filaments as the linkages needed to transmit to the podosome ring the vertical forces necessary to explain talin vertical extension. Thus, our finding that tension is necessary for protrusion reframes the podosome ring as an assembly of adhesion complexes that would operate, individually, as small-scale focal adhesions; but collectively, these complexes would counterbalance the polymerizing force of the actin core they encircle, ultimately resulting in orthogonal deformation of the substrate. The interaction of actin with traction-associated proteins, namely, talin, vinculin, and paxillin, may also explain why podosomes are mechanoresponsive, as reported previously:[6] mechanosensing would be operated by the ring and its lateral filaments in the same way as it occurs in focal adhesion and stress fibers. Finally, we are led to the idea that two different subcellular structures using the same set of components with the same molecular mechanisms, but organized each with its own specific architecture, acquire different mesoscopic abilities, *i.e.*, pull on, or protrude into, the substrate. It may be that such versatility corresponds to different environments encountered by the migrating cell[35] or by different cell types adapted to varying matrix properties.

CONCLUSION

This study reveals feedback at a submicrometer scale between force-generating machinery and adhesion components. Our approach highlights the fruitfulness of a combined mechanical and architectural approach to dissect the workings of active biological structures inside the cell. Zooming out from podosomes, this work sheds light on the mechanobiology of the actin-based subcellular protrusive structures found in various cell processes, including 3D migration,[11] cancer cell invasion,[2] vascular branching,[3] axon growth,[4] and bone resorption.[5] It also clarifies the similarities to and differences from the well-known adhesion structure, focal adhesions, and advances the understanding of the diverse strategies adopted by cell types to adhere and migrate in their respective environments.

METHODS

Differentiation and Culture of Primary Monocyte-Derived Macrophages. Human monocytes were isolated from blood of healthy donors as described previously.[1] Cells were resuspended in cold phosphate buffer saline (PBS) supplemented with 2 mM EDTA and 0.5% heat-inactivated fetal calf serum (FCS) at pH 7.4 and magnetically sorted with magnetic microbeads coated with antibodies directed against CD14 (Miltenyi Biotec). Monocytes were then seeded on glass coverslips at 1.5×10^6 cells/well in six-well plates in RPMI 1640 (Invitrogen) without FCS. After 2 h at 37 °C in a humidified 5% CO_2 atmosphere, the medium was replaced by RPMI containing 10% FCS and 20 ng/mL of macrophage colony-stimulating factor (M-CSF) (Peprotech). For experiments, cells were harvested at day 7 using trypsin-EDTA (Fisher Scientific) and centrifugation (1000 rpm, 10 min).

RNA Interference Knockdown. Macrophages were transfected at day 7 of differentiation with 166 nM siRNA using the HiPerfect system (Qiagen) as described previously.[21] The mix of HiPerfect and siRNA was incubated for 15 min at room temperature and then added drop by drop to the cells. On the basis of the use of the red siGLO transfection indicator (Dharmacon), this protocol yielded a large delivery of siRNA (95% of siGLO-positive cells). After 10 days with siRNA, macrophages were detached with trypsin-ETDA (Invitrogen) and lysed for Western blot analysis or plated at 2.5×10^4 cells cm^{-2} on Formvar-coated grids or on glass coverslips for microscopy experiments. An approximate 75% protein depletion was obtained (see Results). Cells were monitored randomly; hence our measurements provide the average effect of depletion and may underestimate its actual effect. The following siRNA (Dharmacon) were used: human ON-TARGET plus SMART pool siRNA nontargeting control pool (siCtrl); ON-TARGET plus SMART pool siRNA, TLN1 sequences (talin-1): 5′-GAGAUGAGGAGUCUACUAU-3′; 5′-UCAAUCAGCUCAUCACUAU-3′; 5′-GUAGAGGACCUGACAACAA-3′; 5′-GAAGAUGGUUGGCGGCAUU-3′; ON-TARGET plus SMART pool siRNA, vinculin sequences: 5′-UGAGAUAAUUCGUGUGUUA-3′; 5′-GAGCGAAUCCAACCAUAA-3′; 5′-GCCAAGCAGUGCACAGAUA-3′; 5′-CAGCAUUUUAUUAAGGUUGA-3′; ON-TARGET plus SMART pool siRNA, paxillin sequences: 5′-CAACUGGAAACCACACAUA-3′; 5′-GGACGUGGCACCCUGAACA-3′; 5′-CCAAACGGCCUGUGUUCUU-3′; 5′-UGACGAAAGAGAAGCCUAA-3′.

Primary Antibodies. The following antibodies were used: mouse anti-talin-N (clone 8d4, Sigma-Aldrich T3287, IF 1/500, WB 1/200), goat anti-talin C-20 (Santa Cruz sc-7534, IF 1/50), mouse anti-vinculin clone hvin-1 (Sigma-Aldrich V9131, IF 1/500, WB 1/200), mouse anti-paxillin (BD Biosciences 61005, IF 1/500, WB 1/1000), rabbit anti-phospho-Tyr118-paxillin (Cell Signaling #2541, WB 1/1000), rabbit anti-actin (Sigma-Aldrich A5060, WB 1/40,000), and mouse anti-tubulin (Sigma-Aldrich T5168, WB 1/10,000).

Immunofluorescence. Macrophages plated on glass coverslips for 3 h were fixed for 10 min in 3.7% (wt/vol) paraformaldehyde solution containing 15 mM sucrose in PBS (Fisher Scientific) at room temperature. When indicated, before fixation, cells were unroofed using distilled water containing cOmplete protease inhibitors (Roche) and 10 μg/mL phalloidin (Sigma-Aldrich P2141) at 37 °C for 30 s. After fixation, cells were permeabilized for 10 min with PBS/0.3% Triton and blocked with PBS/0.3% Triton/1% BSA. Samples were incubated with the primary antibodies for 1 h and then with phalloidin and secondary antibodies for F-actin and ring proteins, respectively.

Finite Element Simulations. Simulations of substrate deformation by podosomes were performed using the Structural Mechanics module of COMSOL Multiphysics 4.3 software (COMSOL France) as described previously.[10] Briefly, a circular Formvar sheet of diameter 16 μm and thickness 30 nm was clamped at its borders. On its lower surface, we defined an array of two-component modules composed of a central disc (radius 140 nm) and a concentric ring (radius 350 nm and width 200 nm) and placed 1.75 μm apart (center-to-center distance). Protrusion at the core was modeled as an upward force of F_p = 10 nN exerted on each disc domain, and local traction consisted of a downward force of $F_t = -(1 + \alpha)F_p$ exerted on each ring domain (Figure 1F,I). The correction factor $\alpha = 10^{-3}$ was chosen empirically so that the seven central bulges were in the same plane. Global traction was modeled as a downward force of $37F_t$ applied either on the periphery (Figure 1D,G) or on the whole area except for a 250-nm-wide disc domain around each core (Figure 1E,H). Meshing used COMSOL default tetrahedral configuration with sizes determined so that the smallest distance spanned at least two tetrahedrons.

Protrusion Force Microscopy. Protrusion force measurements were performed as described previously.[6,10] Briefly, AFM measurements were performed using silicon nitride cantilevers (MLCT-AUHW, Veeco Instruments) with a nominal spring constant of 0.01 N/m mounted on a NanoWizard III AFM (JPK Instruments) coupled to an inverted optical microscope (Axiovert 200, Carl Zeiss). The cantilever sensitivity and spring constant were calibrated before each experiment with the JPK Instruments software using the thermal noise

DOI: 10.1021/acsnano.7b00622
ACS Nano 2017, 11, 4028−4040

method.[36] To prepare Formvar sheets, ethanol-cleaned glass slides were dipped into a Formvar solution of 0.5% (w/v) ethylene dichloride (Electron Microscopy Science) for a few seconds, and the solution was emptied from the film-casting device using a calibrated flow. A Formvar film was detached from dried slides by contact with water and was left floating at the surface. Acetone-washed 200-mesh nickel grids (EMS) were arranged on the floating film, picked up, coated with the film onto another glass slide, and then air-dried. To evaluate the thickness of the Formvar sheet, the border of the Formvar that remained on the glass slide after removing the grids was imaged in contact mode by AFM. Living cells were plated on Formvar-coated grids that were placed inside a temperature-controlled chamber (Petri dish heater, JPK Instruments), and the culture medium was supplemented with 10 mM HEPES (pH = 7.4) (Sigma-Aldrich). For the inhibition of paxillin phosphorylation, PFM was performed on the same cells before and after 30 min treatment with the FAK inhibitor PF-562,271 (Euromedex) at 1.5 μg/mL. Images were recorded in contact mode in liquid at scanning forces lower than 1 nN. Cell-induced protrusions were imaged with a pixel resolution of 256 or 512 pixels at a line rate around 2 Hz. Forces exerted by single podosomes were derived from the topographical data of podosome-induced protrusions,[10] and each cell was attributed the median force value of its podosomes. Briefly, the deformation profile of each protrusion was measured on the AFM image using an ImageJ macro and, combined with the ring radius values, led to the determination of the deformation height h. This was converted to force for each podosome by the relation $F = C_0 \frac{E}{1-\nu^2} \frac{h_f^3}{r_t^2} h$, where the biaxial Young's modulus of Formvar, $E/(1-\nu^2)$, is 2.3 GPa (ref 6), $C_0 \approx 2.7$ is a geometric coefficient evaluated from numerical simulations,[10] and the film thickness h_f and ring radius r_t were measured for each series of experiments by AFM and immunofluorescence, respectively.

FRAP Measurements. Macrophages were transfected with mRFP-actin (kindly provided by S. Linder) using the Neon electroporation system (Invitrogen) as described previously[37] and plated in a Lab-Tek glass-bottom chamber (Fisher Scientific) 6 h before experiment. FRAP was performed on a LSM710 confocal microscope (Zeiss) using a dedicated FRAP module included in the ZEN software. The microscope was equipped with a 40×/1.3 oil objective and a 37 °C, 5% CO_2 incubator. The 561 nm laser line was used for both imaging and bleaching. Images were acquired every 5 s with a pixel dwell of 9 μs. Podosomes were delimited by creating circular regions of 1.05 μm diameter and bleached sequentially to obtain a 50 ± 10% decrease in fluorescence. Recovery and control curves (fluorescence intensity extracted from a nonbleached region) were measured with ImageJ and exported and fitted in Excel following the Soumpasis equation.[38] $t_{1/2}$ values were calculated from this fit.

DONALD 3D Super-resolution Imaging. Macrophages plated on glass coverslips of accurate thickness (0.17 mm ± 0.5%, Marienfeld) were unroofed and fixed with 3.7% paraformaldehyde/0.2% glutaraldehyde in PBS. Talin, vinculin, and paxillin were stained with the corresponding primary antibody and an Alexa Fluor 647-coupled secondary antibody (Molecular Probes A21237, 1/1000) for dSTORM, and podosome cores were labeled with Alexa Fluor 488-phalloidin (Molecular Probes A12379, 1/500) for epifluorescence. dSTORM imaging of F-actin was performed on samples stained with Alexa Fluor 647-coupled phalloidin only (Molecular Probes, A22287, 1/200). All dSTORM experiments were performed with the Smart-kit buffer (Abbelight, France).

3D superlocalization images were acquired using a Nikon Eclipse Ti inverted microscope combined with a Perfect Focus System and configured for these studies in HiLo excitation thanks to a homemade optical configuration. Samples were excited with a 488 nm (Genesis MX-STM 500 mW, Coherent) and a 637 nm (Obis 637 LX 140 mW, Coherent) optically pumped semiconductor laser. A set of full-multiband laser filters, optimized for 405, 488, 561, and 635 nm laser sources (LF405/488/561/635-A-000, Semrock), was used to excite Alexa Fluor 488 or 647 for the collection of the resultant fluorescence *via* a Nikon APO 60×/1.49 oil immersion objective lens. All images were recorded using a 512 × 512 pixels EMCCD camera (iXon 897, Andor), split on two regions of 325 × 256-pixel area, and positioned on the focal plane of the DONALD module (2.7× magnification, optical pixel size of 100 nm). The two imaging paths are calibrated in terms of transmission efficiency to define a permanent correction factor that compensates the imperfect beamsplitter.

To induce the majority of the fluorophores into the dark state, we excited the samples using a laser in an oblique configuration. Once the density of fluorescent dye was sufficient (typically, under 1 molecule/μm^2), we activated the real-time three-dimensional localization performed by home-written Python code. For all recorded images, the integration time and the EMCCD gain were set to 50 ms and 150, respectively.

The spatial organization of proteins within the podosome was quantified as follows. First, podosome cores were located as the intensity peaks on actin epifluorescence images from the 488 nm channel after Gaussian filtering, and each was attributed its in-plane coordinates (x_{core}, y_{core}). Then, for each core, the protein molecules distant laterally by less than 1 μm from this core were selected among all molecules detected in the 647 nm channel (*i.e.*, the points (x_i, y_i, z_i) such that $r_i = [(x_i - x_{core})^2 + (y_i - y_{core})^2]^{1/2} < 1$ μm) and counted as points (r_i, z_i) of an r–z space. This analysis was performed for all podosomes of a given cell, which resulted in a correlation of height *versus* radius for each cell. From these data, the average height for each distance class (radial height profiles shown in Figures 4D,E and 5D) was determined by fitting the height distribution within the class with a Gaussian distribution and taking the peak height. Finally, the average height given in the text was calculated as the average over all distance classes ($200 \le r < 800$ nm) weighed by the radial density (see data in Table S4).

To determine the 3D molecular organization of each protein, we generated radial density maps and located each protein with respect to the center of the podosome. Experimentally, through the combination of dSTORM and SAF, we have access to the number of detected proteins dn(x, y, z) in an infinitesimal volume given by the x, y- and z-resolution of the technique. In cylindrical coordinates, this number transforms into dn(r, z) by changing the x, y coordinates into the lateral distance r to the center of the podosome core and can be expressed as $\mathrm{dn}(r, z) = \alpha 2\pi r\, f(r, z)\, \mathrm{d}r\, \mathrm{d}z$. In this expression, $f(r, z)$ represents the probability density of the height and radius of each labeled protein around the core, which we call the radial height probability density of the protein, and α is a normalization coefficient ensuring that the total probability is equal to 1, *viz.*, $\int\int f(r, z) 2\pi r\, \mathrm{d}r\, \mathrm{d}z = 1$. Figures 4C and 5C) represent this radial height probability density as a probabilistic density map for each labeled protein: $f(r, z)$ was determined for all the podosomes of a given cell, then averaged over all investigated cells per donor and then over all donors, as described in Figure 3D. Briefly, each protein molecule of coordinates (x_i, y_i, z_i) detected around a given podosome core (x_{core},y_{core}) was plotted on an r–z graph at coordinates (r_i, z_i) with an intensity of $1/r_i$, the superposition of which yielded, after normalization, the graph of $f(r, z)$ for this podosome. The graphs were averaged over more than 50 podosomes per cell, then over all cells per donor, and finally over all donors. Finally, the radial height probability density was shown as a density map, each region of which is determined as the region of smallest area that encloses a given proportion of the proteins.

Confocal Imaging. For analysis of talin, vinculin, and paxillin podosome content shown in Figure S2B,D,F, siTln, siVinc, or siPax cells were plated on glass coverslips together with siCtrl cells previously stained with Cell Tracker Green (CMFDA, Molecular Probes). Mixed cell populations were fixed and processed for immunofluorescence using Atto 390-phalloidin (Sigma, 1/200) for F-actin and the Alexa Fluor 555-coupled secondary antibody (Molecular Probes, 1/1000) for ring proteins. Confocal images were acquired using a 60×/1.4 objective on an Olympus FV1000 microscope. Podosomes were analyzed with Fiji software. Briefly, podosome cores were detected using the "Find Maxima" function of the software. After subtraction of the mean fluorescent background, the mean fluorescent intensity was measured in a 1.5-μm-large circular region centered on the core. For each field of view, intensity

DOI: 10.1021/acsnano.7b00622
ACS Nano 2017, 11, 4028–4040

measurements were normalized by the average intensity of the ring component in the siCtrl population.

Deconvolution Imaging. For podosome size measurement, unroofed macrophages immunostained for actin (Texas-Red phalloidin, Molecular Probes T7471, 1/500) and vinculin/paxillin (Alexa Fluor 488 secondary antibody, Molecular Probes M4409, 1/1000) were imaged over nine planes at 100 nm intervals with a 100×/1.45 objective mounted on a Nikon Eclipse Ti-E and an Andor sCMOS Neo camera in high dynamic mode and in global shutter. These images were processed by nonlinear deconvolution as described previously[10] using the ImageJ software Deconvolution Lab.[39] The point spread function (PSF) used for inversion was determined as an average of 30 experimental PSFs. Podosome size was measured automatically from pairs of deconvolved fluorescence images of actin and vinculin or paxillin using a dedicated ImageJ macro.[10] Briefly, the position of the center of each core was determined as the coordinates of the actin intensity peaks weighted by the surrounding gray values. Then radial intensity profiles of vinculin/paxillin rings served to measure the distance from the core to the point of highest vinculin/paxillin intensity. For each podosome, the final value was chosen as the median value of the radii measured in eight directions from the center (each 45° angle).

Podosome Stability Measurements. Macrophages were transduced with mCherry-LifeAct lentiviral vector 2 or 3 days before experiments. Transduction was performed by incubating cells with lentiviral vector (MOI: 1:1) in 800 μL of RMPI 1640 supplemented with 50 μg/mL protamine sulfate. After 2 h at 37 °C, 1.5 mL of fresh RPMI containing 10% FCS and 50 ng/mL M-CSF was added and renewed the day after transduction. For observation, cells were detached and seeded in Lab-Tek glass-bottom chambers. After 4 h, cells were imaged using an inverted microscope (DMIRB, Leica Microsystems) equipped with a 37 °C and 5% CO_2 incubator (Box-Cube-Brick, Life Imaging Systems). Images were acquired with the Metamorph software every 20 s over a 45 min period on 10 representative fields per condition for each experiment. Podosome stability was evaluated by quantifying the median lifespan from 10 manually tracked podosomes per cell.

Western Blot. Cells in six-well plates were detached with trypsin-EDTA (Invitrogen), centrifuged, and then lysed by adding 100 μL of boiling 2× Laemmli buffer containing phosphatase inhibitors (2 mM orthovanadate, 5 mM NaF) onto cell pellets for 5 min. A 20 μg amount of protein was subjected to electrophoresis in 10% SDS−PAGE gels and transferred onto a nitrocellulose membrane. Membranes were saturated with 3% BSA in TBS-T (50 mM Tris, pH 7.2; 150 mM NaCl; and 0.1% Tween 20) for 30 min and incubated with primary antibody overnight at 4 °C. Then, primary antibodies were revealed using a HRP-coupled secondary anti-mouse (Sigma) or anti-rabbit (Cell Signaling Technology, Beverly, MA, USA) antibody for 1 h. Finally, HRP activity was revealed using an electrochemiluminescence kit (Amersham) according to the manufacturer's instructions. All blots were normalized against actin or tubulin expression.

Statistical Analysis. All box-and-whisker plots show the median, lower, and upper quartiles (box) and the 10th and 90th percentiles (whiskers). The median podosome force per cell followed a Gaussian distribution in each condition, as assessed by the D'Agostino−Pearson test. Its variance was similar between each condition. In depletion experiments, the significance of force values was assessed in depleted cells *versus* control cells (Figures 2F and S1E) using the two-tailed unpaired Student's *t*-test. In FAK inhibition experiments (Figure S5D), force values before and after treatment were paired for each cell and compared to each other using the two-tailed paired Student's *t*-test. The slope of height profiles (Figures 4D and 5D,F) was assessed for statistical significance by comparing the height in each distance class to that in the [800; 1000] nm class. Height values were paired within each cell and compared using the two-tailed Wilcoxon's signed-rank test. The height of talin-N *versus* talin-C (Figure 4D was compared within each distance class using the two-tailed Mann−Whitney test. The height of vinculin in depleted *versus* control cells (Figure 5F) was compared within each distance class using the two-tailed Mann−Whitney test. Ring protein intensity (Figure S2B,D,F), cell spreading area (Figure S3B), podosome stability (Figure S4A,B), podosome size (Figure S4C), and fluorescence recovery half-time (Figures 2C and S4B) data were compared between depleted cells and control cells using the two-tailed Mann−Whitney test. In all cases * and # correspond to $p < 0.05$, ** and ## to $p < 0.01$, and *** and ### to $p < 0.001$. See Tables S1−9 for detailed information.

ASSOCIATED CONTENT

Supporting Information

The Supporting Information is available free of charge on the ACS Publications website at DOI: 10.1021/acsnano.7b00622.

Additional figures and tables of numerical data and statistics corresponding to all experiments (PDF)

Dynamics of substrate deformation by podosomes of living cells (AVI)

Effect of depletion on podosome stability (AVI)

AUTHOR INFORMATION

Corresponding Authors

*E-mail: isabelle.maridonneau-parini@ipbs.fr.

*E-mail: renaud.poincloux@ipbs.fr.

ORCID

Renaud Poincloux: 0000-0003-2884-1744

Author Contributions

△A. Bouissou and A. Proag contributed equally to this work.

Author Contributions

¶I. Maridonneau-Parini and R. Poincloux share senior authorship.

Author Contributions

A.B., R.P., and I.M.P. designed the study. A.B., A.P., R.P., and I.M.P. designed the experiments. A.B. set up protein depletion in primary macrophages, performed most of the experiments, and analyzed the data. R.P. and A.P. performed live imaging and FRAP experiments and analyzed the data. N.B. and C.C. carried out DONALD imaging, and N.B. analyzed the data. A.P. performed numerical simulations and designed automated methods to process data sets. G.D., E.F., and S.L.F. provided expertise in super-resolution imaging. C.V. and C.T. helped set up AFM experiments and analyze the data. K.P. prepared macrophages from blood monocytes and performed immunoblotting. S.B. prepared the Formvar-coated grids for PFM. T.M. set up image deconvolution. A.B., A.P., N.B., R.P., and I.M.P. interpreted the results. A.B., A.P., R.P., and I.M.P. wrote the manuscript with input from the other authors. A.B. and A.P. contributed equally to this work.

Notes

The authors declare no competing financial interest.

ACKNOWLEDGMENTS

The authors are grateful to S. Tournier for granting access to her Nikon Eclipse microscope and to G. Giannone, C. Le Clainche, A. Peixoto, B. Raynaud-Messina, and C. Vérollet for helpful discussions and critical reading of the manuscript. The authors also acknowledge the TRI imaging facility. This work has been supported in part by l'Agence Nationale de la Recherche (ANR 2010-01301, ANR14-CE11-0020-02, ANR-11-EMMA-0047, ANR-10-LABX-24, and ANR-10-IDEX-0001-02 PSL*), la Fondation pour la Recherche Médicale (FRM DEQ2016 0334894), INSERM Plan Cancer, Fondation Toulouse Cancer, AXA Research Fund, DIM NanoK, and Human Frontier Science Program (RGP0035/2016).

DOI: 10.1021/acsnano.7b00622
ACS Nano 2017, 11, 4028−4040

REFERENCES

(1) Van Goethem, E.; Poincloux, R.; Gauffre, F.; Maridonneau-Parini, I.; Le Cabec, V. Matrix Architecture Dictates Three-Dimensional Migration Modes of Human Macrophages: Differential Involvement of Proteases and Podosome-Like Structures. *J. Immunol.* **2010**, *184*, 1049−1061.

(2) Lizarraga, F.; Poincloux, R.; Romao, M.; Montagnac, G.; Le Dez, G.; Bonne, I.; Rigaill, G.; Raposo, G.; Chavrier, P. Diaphanous-Related Formins Are Required for Invadopodia Formation and Invasion of Breast Tumor Cells. *Cancer Res.* **2009**, *69*, 2792−2800.

(3) Seano, G.; Chiaverina, G.; Gagliardi, P. A.; di Blasio, L.; Puliafito, A.; Bouvard, C.; Sessa, R.; Tarone, G.; Sorokin, L.; Helley, D.; Jain, R. K.; Serini, G.; Bussolino, F.; Primo, L. Endothelial Podosome Rosettes Regulate Vascular Branching in Tumour Angiogenesis. *Nat. Cell Biol.* **2014**, *16*, 931−941 931−938.

(4) Santiago-Medina, M.; Gregus, K. A.; Nichol, R. H.; O'Toole, S. M.; Gomez, T. M. Regulation of ECM Degradation and Axon Guidance by Growth Cone Invadosomes. *Development* **2015**, *142*, 486−496.

(5) Jurdic, P.; Saltel, F.; Chabadel, A.; Destaing, O. Podosome and Sealing Zone: Specificity of the Osteoclast Model. *Eur. J. Cell Biol.* **2006**, *85*, 195−202.

(6) Labernadie, A.; Bouissou, A.; Delobelle, P.; Balor, S.; Voituriez, R.; Proag, A.; Fourquaux, I.; Thibault, C.; Vieu, C.; Poincloux, R.; Charrière, G. M.; Maridonneau-Parini, I. Protrusion Force Microscopy Reveals Oscillatory Force Generation and Mechanosensing Activity of Human Macrophage Podosomes. *Nat. Commun.* **2014**, *5*, 5343.

(7) Linder, S.; Wiesner, C. Tools of the Trade: Podosomes as Multipurpose Organelles of Monocytic Cells. *Cell. Mol. Life Sci.* **2015**, *72*, 121−135.

(8) Zhang, X.; Jiang, G.; Cai, Y.; Monkley, S. J.; Critchley, D. R.; Sheetz, M. P. Talin Depletion Reveals Independence of Initial Cell Spreading from Integrin Activation and Traction. *Nat. Cell Biol.* **2008**, *10*, 1062−1068.

(9) Plotnikov, S. V.; Pasapera, A.; Sabass, B.; Waterman, C. M. Force Fluctuations within Focal Adhesions Mediate Ecm Rigidity Sensing to Guide Directed Cell Migration. *Cell* **2012**, *23*, 151310.1016/j.cell.2012.11.034.

(10) Proag, A.; Bouissou, A.; Mangeat, T.; Voituriez, R.; Delobelle, P.; Thibault, C.; Vieu, C.; Maridonneau-Parini, I.; Poincloux, R. Working Together: Spatial Synchrony in the Force and Actin Dynamics of Podosome First Neighbors. *ACS Nano* **2015**, *9*, 3800−3813.

(11) Van Goethem, E.; Guiet, R.; Balor, S.; Charriere, G. M.; Poincloux, R.; Labrousse, A.; Maridonneau-Parini, I.; Le Cabec, V. Macrophage Podosomes Go 3D. *Eur. J. Cell Biol.* **2011**, *90*, 224−236.

(12) Ciobanasu, C.; Faivre, B.; Le Clainche, C. Actomyosin-Dependent Formation of the Mechanosensitive Talin-Vinculin Complex Reinforces Actin Anchoring. *Nat. Commun.* **2014**, *5*, 3095.

(13) del Rio, A.; Perez-Jimenez, R.; Liu, R. C.; Roca-Cusachs, P.; Fernandez, J. M.; Sheetz, M. P. Stretching Single Talin Rod Molecules Activates Vinculin Binding. *Science* **2009**, *323*, 638−641.

(14) Yao, M.; Goult, B. T.; Chen, H.; Cong, P.; Sheetz, M. P.; Yan, J. Mechanical Activation of Vinculin Binding to Talin Locks Talin in an Unfolded Conformation. *Sci. Rep.* **2014**, *4*, 4610.

(15) Atherton, P.; Stutchbury, B.; Wang, D. Y.; Jethwa, D.; Tsang, R.; Meiler-Rodriguez, E.; Wang, P.; Bate, N.; Zent, R.; Barsukov, I. L.; Goult, B. T.; Critchley, D. R.; Ballestrem, C. Vinculin Controls Talin Engagement with the Actomyosin Machinery. *Nat. Commun.* **2015**, *6*, 10038.

(16) Case, L. B.; Baird, M. A.; Shtengel, G.; Campbell, S. L.; Hess, H. F.; Davidson, M. W.; Waterman, C. M. Molecular Mechanism of Vinculin Activation and Nanoscale Spatial Organization in Focal Adhesions. *Nat. Cell Biol.* **2015**, *17*, 880−892.

(17) Calderwood, D. A.; Campbell, I. D.; Critchley, D. R. Talins and Kindlins: Partners in Integrin-Mediated Adhesion. *Nat. Rev. Mol. Cell Biol.* **2013**, *14*, 503−517.

(18) Deakin, N. O.; Turner, C. E. Paxillin Comes of Age. *J. Cell Sci.* **2008**, *121*, 2435−2444.

(19) Zaidel-Bar, R.; Itzkovitz, S.; Ma'ayan, A.; Iyengar, R.; Geiger, B. Functional Atlas of the Integrin Adhesome. *Nat. Cell Biol.* **2007**, *9*, 858−867.

(20) Pasapera, A. M.; Schneider, I. C.; Rericha, E.; Schlaepfer, D. D.; Waterman, C. M. Myosin II Activity Regulates Vinculin Recruitment to Focal Adhesions through FAK-Mediated Paxillin Phosphorylation. *J. Cell Biol.* **2010**, *188*, 877−890.

(21) Troegeler, A.; Lastrucci, C.; Duval, C.; Tanne, A.; Cougoule, C.; Maridonneau-Parini, I.; Neyrolles, O.; Lugo-Villarino, G. An Efficient siRNA-Mediated Gene Silencing in Primary Human Monocytes, Dendritic Cells and Macrophages. *Immunol. Cell Biol.* **2014**, *92*, 699−708.

(22) Roberts, W. G.; Ung, E.; Whalen, P.; Cooper, B.; Hulford, C.; Autry, C.; Richter, D.; Emerson, E.; Lin, J.; Kath, J.; Coleman, K.; Yao, L.; Martinez-Alsina, L.; Lorenzen, M.; Berliner, M.; Luzzio, M.; Patel, N.; Schmitt, E.; LaGreca, S.; Jani, J.; et al. Antitumor Activity and Pharmacology of a Selective Focal Adhesion Kinase Inhibitor, PF-562,271. *Cancer Res.* **2008**, *68*, 1935−1944.

(23) Kanchanawong, P.; Shtengel, G.; Pasapera, A. M.; Ramko, E. B.; Davidson, M. W.; Hess, H. F.; Waterman, C. M. Nanoscale Architecture of Integrin-Based Cell Adhesions. *Nature* **2010**, *468*, 580−584.

(24) Austen, K.; Ringer, P.; Mehlich, A.; Chrostek-Grashoff, A.; Kluger, C.; Klingner, C.; Sabass, B.; Zent, R.; Rief, M.; Grashoff, C. Extracellular Rigidity Sensing by Talin Isoform-Specific Mechanical Linkages. *Nat. Cell Biol.* **2015**, *17*, 1597−1606.

(25) Kumar, A.; Ouyang, M.; Van den Dries, K.; McGhee, E. J.; Tanaka, K.; Anderson, M. D.; Groisman, A.; Goult, B. T.; Anderson, K. I.; Schwartz, M. A. Talin Tension Sensor Reveals Novel Features of Focal Adhesion Force Transmission and Mechanosensitivity. *J. Cell Biol.* **2016**, *213*, 371−383.

(26) Bourg, N.; Mayet, C.; Dupuis, G.; Barroca, T.; Bon, P.; Lecart, S.; Fort, E.; Lévêque-Fort, S. Direct Optical Nanoscopy with Axially Localized Detection. *Nat. Photonics* **2015**, *9*, 587.

(27) Deschamps, J.; Mund, M.; Ries, J. 3D superresolution microscopy by supercritical angle detection. *Opt. Express* **2014**, *22*, 29081−29091.

(28) Campbell, I. D.; Humphries, M. J. Integrin Structure, Activation, and Interactions. *Cold Spring Harbor Perspect. Biol.* **2011**, *3*, a00499410.1101/cshperspect.a004994.

(29) Liu, J.; Wang, Y.; Goh, W. I.; Goh, H.; Baird, M. A.; Ruehland, S.; Teo, S.; Bate, N.; Critchley, D. R.; Davidson, M. W.; Kanchanawong, P. Talin Determines the Nanoscale Architecture of Focal Adhesions. *Proc. Natl. Acad. Sci. U. S. A.* **2015**, *112*, E4864−4873.

(30) Yao, M.; Goult, B. T.; Klapholz, B.; Hu, X.; Toseland, C. P.; Guo, Y.; Cong, P.; Sheetz, M. P.; Yan, J. The Mechanical Response of Talin. *Nat. Commun.* **2016**, *7*, 11966.

(31) Gingras, A. R.; Ziegler, W. H.; Frank, R.; Barsukov, I. L.; Roberts, G. C. K.; Critchley, D. R.; Emsley, J. Mapping and Consensus Sequence Identification for Multiple Vinculin Binding Sites within the Talin Rod. *J. Biol. Chem.* **2005**, *280*, 37217−37224.

(32) van den Dries, K.; Meddens, M. B.; de Keijzer, S.; Shekhar, S.; Subramaniam, V.; Figdor, C. G.; Cambi, A. Interplay between Myosin IIa-Mediated Contractility and Actin Network Integrity Orchestrates Podosome Composition and Oscillations. *Nat. Commun.* **2013**, *4*, 1412.

(33) Proag, A.; Bouissou, A.; Vieu, C.; Maridonneau-Parini, I.; Poincloux, R. Evaluation of the Force and Spatial Dynamics of Macrophage Podosomes by Multi-Particle Tracking. *Methods* **2016**, *94*, 75−84.

(34) Gawden-Bone, C.; Zhou, Z.; King, E.; Prescott, A.; Watts, C.; Lucocq, J. Dendritic Cell Podosomes Are Protrusive and Invade the Extracellular Matrix Using Metalloproteinase MMP14. *J. Cell Sci.* **2010**, *123*, 1427−1437.

(35) Yu, C. H.; Rafiq, N. B.; Krishnasamy, A.; Hartman, K. L.; Jones, G. E.; Bershadsky, A. D.; Sheetz, M. P. Integrin-Matrix Clusters Form Podosome-Like Adhesions in the Absence of Traction Forces. *Cell Rep.* **2013**, *5*, 1456−1468.

DOI: 10.1021/acsnano.7b00622
ACS Nano 2017, 11, 4028−4040

(36) Hutter, J. L.; Bechhoefer, J. Calibration of Atomic-Force Microscope Tips. *Rev. Sci. Instrum.* **1993**, *64*, 1868−1873.
(37) Wiesner, C.; Faix, J.; Himmel, M.; Bentzien, F.; Linder, S. KIF5b and KIF3a/KIF3b Kinesins Drive MT1-MMP Surface Exposure, CD44 Shedding, and Extracellular Matrix Degradation in Primary Macrophages. *Blood* **2010**, *116*, 1559−1569.
(38) Soumpasis, D. M. Theoretical-Analysis of Fluorescence Photobleaching Recovery Experiments. *Biophys. J.* **1983**, *41*, 95−97.
(39) Vonesch, C.; Unser, M. A Fast Thresholded Landweber Algorithm for Wavelet-Regularized Multidimensional Deconvolution. *IEEE Trans. Image Process.* **2008**, *17*, 539−549.
(40) Enderlein, J.; Gregor, I.; Ruckstuhl, T. Imaging Properties of Supercritical Angle Fluorescence Optics. *Opt. Express* **2011**, *19*, 8011−8018.

NOTE ADDED AFTER ASAP PUBLICATION

This manuscript published ASAP on 4/4/2017. A missing reference citation was added and the revised version was reposted on 4/14/2017.

DOI: 10.1021/acsnano.7b00622
ACS Nano 2017, 11, 4028−4040